Charge Separation Measurements in Au+Au collisions at $\sqrt{s_{NN}}$ = 7.7–200 GeV in Search of the Chiral Magnetic Effect*

The STAR Collaboration

Abstract: The chiral magnetic effect in heavy-ion collisions predicts an electric charge separation along the direction of a strong magnetic field, which indicates local parity ($\mathcal{P}$) and charge-conjugation-parity ($\mathcal{CP}$) violations in strong interactions. We report measurements of electric charge separation signals perpendicular to the spectator event plane in Au+Au collisions using high-statistics data from RHIC Beam Energy Scan II and top-RHIC energy ($\sqrt{s_{NN}} = 200$ GeV) runs. A novel event shape selection method is employed to suppress the flow-induced background. The residual charge-separation signal fractions near the zero-flow limit are positive in Au+Au collisions within the 20%–50% centrality range. The significance levels are 2.8σ, 3σ, and 3.2σ at $\sqrt{s_{NN}}$ = 11.5, 14.6, and 19.6 GeV, respectively. At other beam energies, the signals are either statistically limited or consistent with zero.

Keywords: heavy-ion collision, chiral magnetic effect, chiral anomaly

DOI: **CSTR:**

I. INTRODUCTION

The search for parity ($\mathcal{P}$) and charge-conjugation-parity ($\mathcal{CP}$) symmetry violation in non-Abelian gauge theories, such as quantum chromodynamics (QCD), which describes the strong interaction, remains one of the central challenges in modern physics. The chiral magnetic effect (CME) provides a possible manifestation of such symmetry violation in high-energy systems, predicting the induction of an electric current ($\vec{J}$) along the direction of an intense magnetic field ($\vec{B}$) due to a finite chirality chemical potential ($\mu_5 \neq 0$), as originally discussed for a quark–gluon plasma (QGP) [1−3], while analogous realizations arise in condensed-matter systems. This phenomenon, $\vec{J} \propto \mu_5 \vec{B}$, has been experimentally confirmed in topological materials such as Dirac [4, 5] and Weyl [6] semimetals, where μ_5 and $\vec{B}$ can be engineered and controlled. The CME in the strong force is more elusive [7, 8], as its formation requires synchronizing several preconditions in a fast-evolving system, and detecting it demands eliminating intricate backgrounds. Nevertheless, observing the CME in QCD matter would provide direct insight into the topological structure of the QCD vacuum and the role of anomalous chiral transport in strongly interacting matter.

Heavy-ion collisions at the BNL Relativistic Heavy Ion Collider (RHIC) and the CERN Large Hadron Collider (LHC) can create a deconfined QGP, whose physical conditions are theorized to have existed microseconds after the Big Bang [9−14]. Chiral symmetry restoration is anticipated to accompany deconfinement, whereby light quarks become nearly massless and bear definite chirality. Figure 1 depicts a possible chirogenesis mechanism in which collective gluon excitations generate topological vacuum transitions, transferring net chirality to (anti)quarks within the rapidly expanding QGP droplets [1−3]. This chirogenesis in the strong interaction is a prerequisite for the CME, and if observed, could serve as an analogous mechanism for understanding baryogenesis in the electroweak interaction of the early Universe [7].

Over the past two decades, extensive experimental efforts at RHIC and the LHC have searched for the CME using charge-dependent azimuthal correlations [15−20]. Although finite electric charge separation signals have

Received 2 July 2026; Accepted 22 July 2026

* This work was supported in part by the Office of Nuclear Physics within the U.S. DOE Office of Science, the U.S. National Science Foundation, National Natural Science Foundation of China, Chinese Academy of Science, the Ministry of Science and Technology of China and the Chinese Ministry of Education, NSTC Taipei, the National Research Foundation of Korea, Czech Science Foundation and Ministry of Education, Youth and Sports of the Czech Republic, Hungarian National Research, Development and Innovation Office, New National Excellency Programme of the Hungarian Ministry of Human Capacities, Department of Atomic Energy and Department of Science and Technology of the Government of India, the National Science Centre and WUT ID-UB of Poland, the Ministry of Science, Education and Sports of the Republic of Croatia, German Bundesministerium für Bildung, Wissenschaft, Forschung and Technologie (BMBF), Helmholtz Association, Ministry of Education, Culture, Sports, Science, and Technology (MEXT), Japan Society for the Promotion of Science (JSPS) and Agencia Nacional de Investigación y Desarrollo (ANID) of Chile

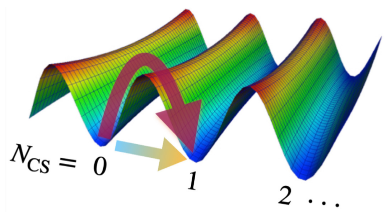

Fig. 1. (color online) Schematic diagram illustrating the potential energy in gluon fields. The straight and curved arrows represent two modes of topological vacuum transitions in QCD, marked by a change in the Chern-Simons number (N_{CS}).

been observed, their interpretation remains ambiguous, as the measurements are dominated by background correlations associated with collective flow and other conventional physics mechanisms[21−23]. Therefore, disentangling a possible CME signal from these dominant backgrounds remains the central challenge in experimental searches for the CME in heavy-ion collisions. In this work, we report the recent STAR measurements of charge separation in Au+Au collisions across the RHIC Beam Energy Scan phase II (BES-II) program and at the top RHIC energy ($\sqrt{s_{NN}} = 200$ GeV). By employing a novel event-shape-selection method, this work aims to suppress background contributions and isolate the possible CME signal. Additional technical details can be found in a recent STAR paper [24].

II. DETECTION OF THE CME

A typical noncentral heavy-ion collision, with two nuclei passing each other at nearly the speed of light, is illustrated in Figure 2. The resulting magnetic field, perpendicular to the reaction plane (the x-z plane), is estimated to peak around $10^{17} - 10^{19}$ Gauss [25, 26]. With nonzero μ_5 in the participant zone, the CME could thus yield an electric charge separation orthogonal to the reaction plane from (anti)quarks in metastable domains. Though the transient magnetic field is among the strongest in the cosmos, its impact on final-state particles is difficult to detect due to its rapid decay.

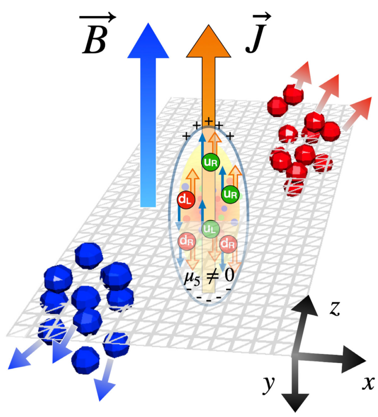

Fig. 2. (color online) Sketch of the CME in a two-nucleus collision. The forward- and backward-moving nucleon groups denote spectator nucleons that do not participate in the collision but contribute to a strong magnetic field $\vec{B}$. In the participant zone (the overlap region), the CME induces an electric current ($\vec{J}$) across the x-z plane in chiral domains ($\mu_5 \neq 0$).

A. Observable and Early Measurements

The CME charge separation may be quantified using Fourier coefficients of the azimuthal angle distribution of final-state charged particles. The distribution of positive and negative particles ($N_\pm$) is expressed as a function of the azimuthal angle (φ) relative to the reaction plane (Ψ_{RP}) [21],

$$\frac{dN_\pm}{d\varphi} \propto 1 + \sum_{n=1}^{\infty} 2v_n^\pm \cos n\Delta\varphi + 2a_1^\pm \sin\Delta\varphi, \qquad (1)$$

where $\Delta\varphi = \varphi - \Psi_{RP}$. Hydrodynamic expansion [27] of the system converts the initial overlap geometry into a momentum anisotropy (v_n) of the final-state particles. The a_1^+ and a_1^- bear opposite signs because of charge separation and are of order $1/N$, where N is the particle multiplicity [21]. Since parity can be locally violated but globally conserved in QCD, a CME-sensitive observable is designed to probe the fluctuation of a_1. A recent study [28] affirms the similarity in the key components of different CME-sensitive observables. We focus on the most widely used observable [21],

$$\gamma^{112} \equiv \langle \cos(\varphi_\alpha + \varphi_\beta - 2\Psi_{RP}) \rangle, \qquad (2)$$

where α and β represent charge sign. To isolate the charge-dependent signal, we report the difference $\Delta\gamma^{112} \equiv \gamma^{112}_{OS} - \gamma^{112}_{SS}$, which cancels the charge-independent backgrounds common to opposite-sign (OS) and same-sign (SS) pairs.

A CME signal ($\approx 2|a_1^\pm|^2$) contributes positively to $\Delta\gamma^{112}$, while elliptic flow (v_2) forms a major background by coupling with other mechanisms, including resonance decays [21], local charge conservation (LCC) [22], and transverse momentum conservation (TMC) [23]. The flow-related background complicates the interpretation of the positive $\Delta\gamma^{112}$ data observed in Au+Au collisions at the top RHIC energy [15−17] and in Pb+Pb collisions at the LHC energies [18]. Additionally, nonflow correlations [29] from various sources, including clusters, resonances, jets, and dijets, are unrelated to the reaction plane but can also contribute positively to $\Delta\gamma^{112}$. Nonflow effects can be minimized by reconstructing the reaction plane with spectator information. One recent attempt to mitigate the flow-related background involves exploiting subtle signal differences between two isobaric systems with similar backgrounds, ${}_{44}^{96}$Ru+${}_{44}^{96}$Ru and ${}_{40}^{96}$Zr+${}_{40}^{96}$Zr [30]. A CME signal was not observed in STAR isobar data at $\sqrt{s_{NN}} = 200$ GeV [19, 20], indicating that the background contributions dominate over any potential signal at this center-of-mass energy.

As the signal fraction of $\Delta\gamma^{112}$ may be too subtle in small collision systems at $\sqrt{s_{NN}} = 200$ GeV [31], our focus shifts towards larger collision systems with stronger magnetic fields due to more spectator protons, and we have explored a range of beam energies in the RHIC BES program during 2010–2014 (I) and 2018–2021 (II). To separate the CME signal from the flow-related background, STAR previously employed an observable that explicitly parametrizes the background coupling strength [32]:

$$H(\kappa_{\rm bg}) \equiv (\kappa_{\rm bg} v_2 \delta - \gamma^{112})/(1+\kappa_{\rm bg} v_2), \tag{3}$$

where $\kappa_{\rm bg}$ is an adjustable parameter unknown a priori, and $\delta \equiv \langle\cos(\varphi_\alpha - \varphi_\beta)\rangle$ represents a two-particle correlation. The $\kappa_{\rm bg} v_2 \delta$ represents the flow-related background. With $\kappa_{\rm bg} \approx$ 2–3, the difference $\Delta H \equiv H_{\rm SS} - H_{\rm OS}$ in the 0–60% centrality region of Au+Au collisions tends to vanish at $\sqrt{s_{NN}} = 7.7$ and 200 GeV and remains positive and finite at beam energies in between [32]. Recent STAR data of directed flow (v_1) unveiled the magnetic field's imprint on the QGP in Au+Au collisions, with the effect much stronger at $\sqrt{s_{NN}} = 27$ GeV than at 200 GeV [33]. This suggests that the opportunity to detect the CME may be enhanced using the BES-II data. The BES-II program provides over ten times the statistics of BES-I, with a dedicated detector for reconstructing the spectator plane. At sufficiently low energies, the lack of deconfinement also enables testing for the absence of the CME signal.

The background is primarily due to the emission pattern of final-state particles, influenced by fluctuations in both the initial overlap geometry (eccentricity) and the later-stage expansion of the QGP [34]. The event-shape-based technique seeks to directly subtract the flow-related background by classifying events according to their particle-emission patterns and extrapolating $\Delta\gamma^{112}$ to the limit of vanishing elliptic flow. Some methods of event shape engineering [35–38] construct an event shape variable from a kinematic region excluding particles of interest (POI), relying on long-range flow correlations between these regions. However, longitudinal flow-plane decorrelations can weaken the correlation between the event-shape variable and the measured v_2 [39], and the large extrapolation distance to zero v_2 introduces substantial uncertainties [40]. In this work, we adopt a novel event shape selection (ESS) method [31, 40] that captures both geometric and expansion properties while enabling a more precise extrapolation toward zero v_2 background.

B. Experimental Setup and Data Analysis

1. *Detector and Data Selection*

The STAR detector measures thousands of particles typically produced in heavy-ion collisions over a wide range of beam energies and is used to search for novel signatures of the QGP. The BES-II dataset comprises 60 million Au+Au collision events at $\sqrt{s_{NN}} = 7.7$ GeV (2021), 110 million at 9.2 GeV (2019–2020), 160 million at 11.5 GeV (2020), 230 million at 14.6 GeV (2019), 200 million at 17.3 GeV (2021), 360 million at 19.6 GeV (2019) and 490 million at 27 GeV (2018). An additional 2 billion events at $\sqrt{s_{NN}} = 200$ GeV (2016) provides the top-energy reference. The STAR time projection chamber (TPC) [41] reconstructs charged-particle helices and determines the primary vertex position of each event along the beam direction ($V_{z,\rm TPC}$) and its radial distance from the z axis (V_r). We selected events with $|V_{z,\rm TPC}| < 70$ cm (30 cm for 200 GeV) and $|V_r| < 2$ cm. At 200 GeV, we also required $|V_{z,\rm TPC} - V_{z,\rm VPD}| <$ 3 cm, where $V_{z,\rm VPD}$ was measured by the Vertex Position Detector (VPD) [42]. Events chosen with minimum bias triggers are categorized into centrality classes according to the observed charged-particle multiplicity at midrapidity, following the procedure outlined in Ref. [43]. Outlier events showing multiplicity correlation discrepancies between the TPC and the fast time-of-flight detector [44, 45] are excluded as out-of-time pile-up events.

The POI selection involves a cut on the number of ionization points used in the helix reconstruction ($N_{\rm hits} \geq 15$) to ensure track quality, and another cut on the distance of the closest approach to the primary vertex (DCA < 3 cm) to suppress contributions from weak decays and secondary interactions. The kinematic cuts on pseudorapidity, momentum, and transverse momentum are $|\eta| < 1$, $p < 1.4$ GeV/c, and $p_T > 0.2$ GeV/c, respectively, where the dynamics are known to be dominated by hydrodynamics, as established by years of RHIC experimental measurements [11]. Protons and antiprotons exhibit markedly different collective flows at BES energies [46], and the CME-induced charge separation is expected to differ between baryons and mesons [25]. We therefore exclude (anti)protons from POI by requiring $n\sigma_{\rm p} < -2$. Here, $n\sigma_{\rm p}$ quantifies the difference, in terms of standard deviation, between the measured ionization energy loss in the TPC and its expected value for protons [47]. At $\sqrt{s_{NN}}$=7.7 GeV, where protons are more abundant, we tighten the cuts to $p < 1.3$ GeV/c and $n\sigma_{\rm p} < -2.5$.

2. *Analysis Method*

To detect possible electric-charge separation due to the CME, we utilize the spectator plane, which exhibits a stronger correlation with the magnetic-field direction than the participant plane reconstructed from final-state particles in the participant regions [48, 49]. This choice also reduces nonflow background contributions. The STAR event plane detector (EPD, $2.1 < |\eta| < 5.1$) [50] extends into the forward and backward regions. For collisions at $\sqrt{s_{NN}}$ = 7.7–27 GeV, we construct the spectator plane Ψ^f (Ψ^b) at forward (backward) rapidities using the EPD hits at $|\eta|$ exceeding the beam rapidity, where spectator proton contributions are enriched. For collisions at 200 GeV, where the beam rapidity is large, we instead use the zero degree calorimeter shower-maximum detectors (ZDC-SMD) [51]. We then measure three observables using the spectator planes,

$$v_2 = \langle\cos(2\varphi - \Psi^f - \Psi^b)\rangle / \langle\cos(\Psi^f - \Psi^b)\rangle, \quad (4)$$

$$\gamma^{112} = \langle\cos(\varphi_\alpha + \varphi_\beta - \Psi^f - \Psi^b)\rangle / \langle\cos(\Psi^f - \Psi^b)\rangle, \quad (5)$$

$$\gamma^{132} = \langle\cos(\varphi_\alpha - 3\varphi_\beta + \Psi^f + \Psi^b)\rangle / \langle\cos(\Psi^f - \Psi^b)\rangle. \quad (6)$$

The denominator in Eqs. (4), (5), and (6) compensates for the finite event plane resolution. We employ γ^{132} [52] as a background indicator because it is subject to similar flow-related background mechanisms as γ^{112} [24, 31].

To suppress the flow-related background contributions, we apply the ESS method. As illustrated in Fig. 3(a), the emission pattern varies considerably among events sharing the same eccentricity [34]. The ESS method aims to project the charge separation observable towards isotropically emitting events, requiring the event shape variable to come from the same kinematic region as POI to better incorporate short-range fluctuations [40]. To avoid the self-correlation between v_2 and the event shape variable, we construct the latter using particle pairs of interest (PPOI) rather than individual particles, since the pair-based variable is statistically independent of the single-particle v_2 measurement [40].

$$q^2_{2,\mathrm{PPOI}} = \frac{\left(\sum_{i=1}^{N_{\mathrm{pair}}}\sin 2\varphi_i^{\mathrm{p}}\right)^2 + \left(\sum_{i=1}^{N_{\mathrm{pair}}}\cos 2\varphi_i^{\mathrm{p}}\right)^2}{N_{\mathrm{pair}}(1 + N_{\mathrm{pair}} v^2_{2,\mathrm{pair}})}, \quad (7)$$

where N_{pair} is the number of PPOI in one event. φ_i^{p} denotes the azimuthal angle of the momentum sum for a pair, and $v_{2,\mathrm{pair}} \equiv \langle\cos 2(\varphi^{\mathrm{p}} - \Psi_{\mathrm{RP}})\rangle$ is averaged over all PPOI, regardless of charge, and over all events.

Figures 3(b) and 3(c) demonstrate the ESS approach, depicting $\Delta\gamma^{112}$ and $\Delta\gamma^{132}$, respectively, vs v_2 with events classified by $q^2_{2,\mathrm{PPOI}}$ in the 30%–40% centrality range of Au+Au collisions at $\sqrt{s_{NN}} = 14.6$ GeV. We first use $q^2_{2,\mathrm{PPOI}}$ to categorize events into different subsets j, and in each subset, measure $\Delta\gamma_j^{112}$, $\Delta\gamma_j^{132}$, and $v_{2,j}$. Assuming the flow background is linearly correlated with v_2, we then plot $\Delta\gamma_j^{112}$ and $\Delta\gamma_j^{132}$ against $v_{2,j}$, and perform linear fits to obtain the y-intercepts at zero v_2. The lowest v_2 value is close to zero, facilitating the projection to the zero-flow limit. Finally, we restore the unbiased signals with a small correction, $\Delta\gamma_{\mathrm{ESS}}^{112(132)} = (1-\bar{v}_2)^2\Delta\gamma^{112(132)}|_{v_2=0}$, where $\bar{v}_2$ is the average over all subsets [31, 40, 53].

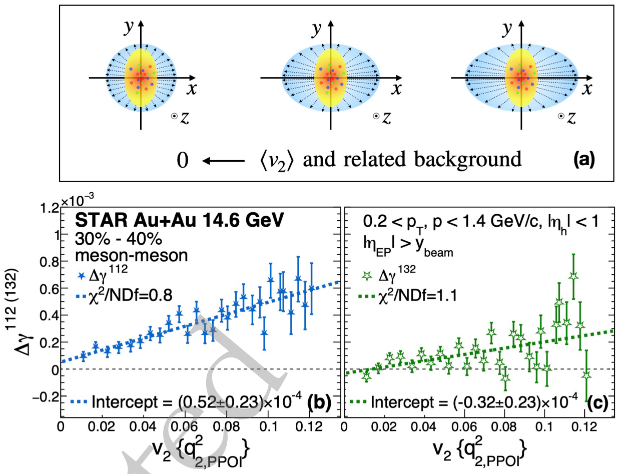

Fig. 3. (color online) (a): illustration of various particle emission patterns (outer regions spanned by arrows) for different events with the same initial geometry (inner elliptic regions). Image reproduced and modified from Ref. [40]. Lower: (b) $\Delta\gamma^{112}$ and (c) $\Delta\gamma^{132}$ as a function of v_2 with events categorized by $q^2_{2,\mathrm{PPOI}}$ in the 30%–40% centrality range of Au+Au collisions at $\sqrt{s_{NN}} = 14.6$ GeV. POI are charged hadrons, excluding (anti)protons. The ESS technique extrapolates an observable to isotropic emission, characterized by zero elliptic flow (v_2). The error bars are statistical only. Linear fits (dashed lines) are used to extract the y-intercepts, with χ^2/NDF close to unity.

Verification of the ESS method in simulation requires a realistic description of the hydrodynamic response during the QGP expansion that links the event-shape variable based on PPOI to the final-state single-particle elliptic flow, along with a reasonably good description of key observables, such as v_2, δ, and $\gamma^{112(132)}$ spectra. Model studies in Ref. [24] show that the hydrodynamics-based EBE-AVFD model [54] successfully reproduces the measured data, demonstrating that such frameworks capture the essential background and thereby supporting the validity of the method [40]. In contrast, transport models such as a multiphase transport model (AMPT) [55] and non-hydrodynamic approaches fail to reproduce key observables [24, 52, 56], and may not fully capture the background in the charge separation measurements. As a result, they may not offer robust closure tests of the event-shaping selection method, and the intercepts extracted from such calculations provide only limited guidance for interpreting the experimental data.

3. *Systematic Uncertainties*

The procedure to assess systematic uncertainties is similar to that used in Ref. [19]. Compound observables, such as centrality-averaged values or the ratio $\Delta\gamma^{112}_{\rm ESS}/\langle\Delta\gamma^{112}\rangle$, are treated as single, unified quantities. We estimate the systematic variation in the observables by making changes in each of the following cuts, $0 < V_{z,\rm TPC} < 70$ cm ($0 < V_{z,\rm TPC} < 30$ cm for 200 GeV), $N_{\rm hits} \geq 20$, DCA < 1 cm, and $n\sigma_{\rm p} < -3$ (-3.5 for 7.7 GeV). Additionally, split tracks are rejected by requiring each accepted track to have the ratio of $N_{\rm hits}$ to the maximum possible number of ionization points greater than 0.52. For each of these cuts, we measure the difference Δ_i between the results with the default cuts and with the varied cuts. For each variation i, we use the Barlow method [57] to account for the impact of statistics. Let $\sigma_{{\rm stat},d}$ and $\sigma_{{\rm stat},i}$ denote the statistical uncertainties for the results with the default and varied cuts, respectively. If Δ_i^2 exceeds $|\sigma^2_{{\rm stat},i} - \sigma^2_{{\rm stat},d}|$, we define $\sigma_i = \sqrt{\Delta_i^2 - |\sigma^2_{{\rm stat},i} - \sigma^2_{{\rm stat},d}|}$. Otherwise, $\sigma_i = 0$. The overall systematic uncertainty is the quadrature sum of $\sigma_i/\sqrt{12}$ (or $\sigma_i/\sqrt{3}$ for the V_z variation), assuming the default and varied-cut results constrain the maximum and minimum, regardless of order, under a flat prior for each source. The final central value is taken as the mean of the averages of these extremes across all five sources [24]. The DCA and $n\sigma_{\rm p}$ cuts are the primary sources of systematic error, each typically at the level of 10% of the corresponding statistical uncertainty. The variations in the rest of the cuts have negligible effects.

III. RESULTS

Figure 4 shows the centrality dependence of (a–h) $N_{\rm part}\Delta\gamma^{112}$ and (i–p) $N_{\rm part}\Delta\gamma^{132}$ in Au+Au collisions at $\sqrt{s_{NN}}$= 7.7–200 GeV. $N_{\rm part}$ denotes the number of participating nucleons [24]. For both observables, the ESS results (circles) exhibit a substantial reduction compared with the ensemble averages (squares). While $N_{\rm part}\Delta\gamma^{132}_{\rm ESS}$ aligns with zero in all centrality intervals at all beam energies, $N_{\rm part}\Delta\gamma^{112}_{\rm ESS}$ is generally finite in mid-central collisions between 10 and 20 GeV. Given the approximately flat centrality dependence in the 20%–50% centrality range, we perform constant fits to improve the statistical precision of the integrated result.

Figure 5(a) presents the beam-energy dependence of $N_{\rm part}\langle\Delta\gamma^{112}\rangle$, $N_{\rm part}\Delta\gamma^{112}_{\rm ESS}$, and $N_{\rm part}\Delta\gamma^{132}_{\rm ESS}$ integrated over the 20%–50% centrality range in Au+Au collisions. The background indicator $\Delta\gamma^{132}_{\rm ESS}$ is consistent with zero at all energies, affirming the effectiveness of flow-related background suppression with the ESS and nonflow background removal with the spectator plane. At $\sqrt{s_{NN}}$= 200 GeV, $\Delta\gamma^{112}_{\rm ESS}$ is consistent with zero. Similar null results have been reported in previous research in Au+Au collisions at this energy [48, 58]. This helps explain why the isobar collisions at $\sqrt{s_{NN}}$= 200 GeV yield a null result. At BES-II energies, the ensemble average $N_{\rm part}\langle\Delta\gamma^{112}\rangle$ remains relatively constant. After the background subtraction, $N_{\rm part}\Delta\gamma^{112}_{\rm ESS}$ reveals a discernible and statistically significant charge separation signal at $\sqrt{s_{NN}}$= 11.5, 14.6, and 19.6 GeV, with significance levels of 2.5σ, 3σ, and 3.2σ, respectively. The remaining charge separation signals are consistent with zero at $\sqrt{s_{NN}}$= 7.7 and 9.2 GeV. The significance levels at $\sqrt{s_{NN}}$= 17.3 and 27 GeV are 1.3σ and 1.1σ, respectively.

Assuming comparable physics conditions between $\sqrt{s_{NN}}$= 10 and 20 GeV, the statistically-weighted average of $N_{\rm part}\Delta\gamma^{112}_{\rm ESS}$ over $\sqrt{s_{NN}}$= 11.5, 14.6, 17.3, and 19.6

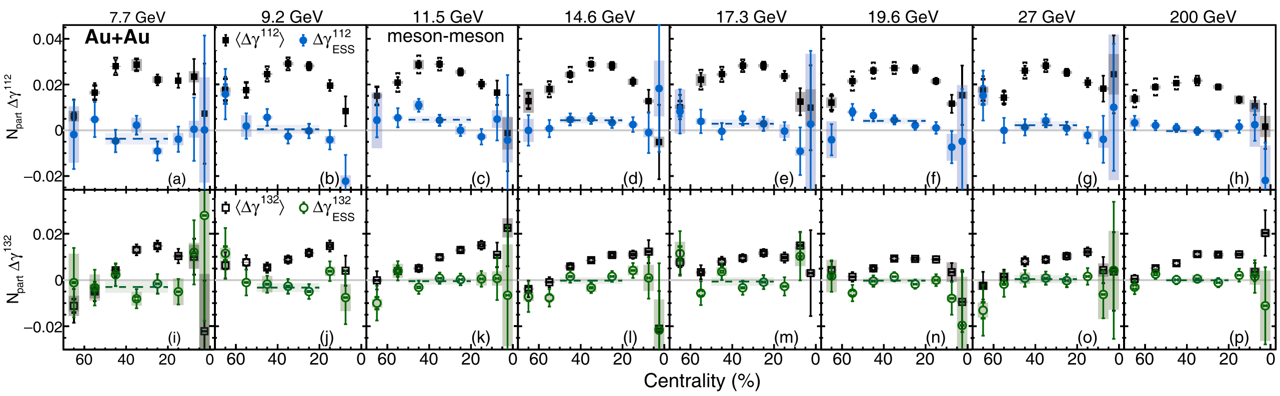

Fig. 4. (color online) Centrality dependence of (a–h) $N_{\rm part}\Delta\gamma^{112}$ and (i–p) $N_{\rm part}\Delta\gamma^{132}$ in Au+Au collisions at $\sqrt{s_{NN}}$= 7.7–200 GeV. Both the ensemble averages (squares) and the ESS results (circles) are presented. The error bars, shaded boxes, and brackets represent statistical uncertainties, measurement systematics, and uncertainties associated with $N_{\rm part}$, respectively. The dashed lines represent constant fits over the 20%–50% centrality range. The shaded bands denote the fit uncertainties.

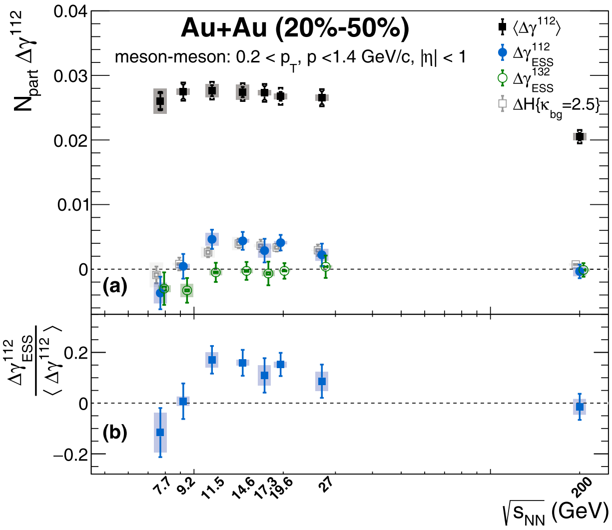

Fig. 5. (color online) (a) Beam-energy dependence of $N_{\rm part}\langle\Delta\gamma^{112}\rangle$ (full squares), $N_{\rm part}\Delta\gamma^{112}_{\rm ESS}$ (full circles), and $N_{\rm part}\Delta\gamma^{132}_{\rm ESS}$ (open circles) integrated over the 20%–50% centrality range in Au+Au collisions. For comparison, we also add the results for $N_{\rm part}\Delta H(\kappa_{\rm bg}=2.5)$ (open squares). (b) The corresponding ratio of $\Delta\gamma^{112}_{\rm ESS}$ to $\langle\Delta\gamma^{112}\rangle$. Some points are slightly shifted horizontally to enhance clarity. The error bars, shaded boxes, and brackets represent statistical uncertainties, measurement systematics, and uncertainties associated with $N_{\rm part}$, respectively.

GeV is $[4.11\pm0.71(stat.)\pm0.23(syst.)\pm0.16(N_{\rm part})]\times10^{-3}$, yielding a 5.4$\sigma$ significance of the charge separation signal. In addition, we find a good agreement between $N_{\rm part}\Delta\gamma^{112}_{\rm ESS}$ and $N_{\rm part}\Delta H(\kappa_{\rm bg}=2.5)$, indicating that the background mechanism can be described with a universal coupling between v_2 and $\Delta\delta\equiv\delta_{\rm OS}-\delta_{\rm SS}$.

Figure 5(b) shows the ratio of $\Delta\gamma^{112}_{\rm ESS}$ to $\langle\Delta\gamma^{112}\rangle$, calculated for each centrality interval from Fig. 4 and then averaged over the 20%–50% centrality range. The ESS method identifies that at least 80% of $\langle\Delta\gamma^{112}\rangle$ arises from the flow-related background. The remaining charge separation signal fractions $\Delta\gamma^{112}_{\rm ESS}/\langle\Delta\gamma^{112}\rangle$ exhibits similar significance levels to $N_{\rm part}\Delta\gamma^{112}_{\rm ESS}$ and are 2.8σ, 3σ, and 3.2σ at $\sqrt{s_{NN}}$= 11.5, 14.6, and 19.6 GeV. This ratio at $\sqrt{s_{NN}}$= 200 GeV is $-0.015\pm0.051(stat.)\pm0.031(syst.)$, compatible with the upper limit of the CME fraction in $\Delta\gamma^{112}$ ($f_{\rm CME}$) reported for isobar collisions [20] and Au+Au collisions [48, 58] at $\sqrt{s_{NN}}$= 200 GeV. At $\sqrt{s_{NN}}$= 27 GeV, the ratio is consistent with the upper limit of $f_{\rm CME}$ estimated from a prior STAR measurement [49].

The prior value $\kappa_{\rm bg}=2.5$ used in Fig. 5(a) is supported by empirical evidence. We estimated the background coupling constants directly from data, under the assumption that the ESS method removes most flow-related background contributions. Replacing H^{112} in Eq. (3) with $\gamma^{112}_{\rm ESS}$, we obtain

$$\kappa^{112}_{\rm bg}=\frac{\Delta\gamma^{112}-\Delta\gamma^{112}_{\rm ESS}}{v_2\left(\Delta\delta+\Delta\gamma^{112}_{\rm ESS}\right)}. \tag{8}$$

Similarly,

$$\kappa^{132}_{\rm bg}=\frac{\Delta\gamma^{132}-\Delta\gamma^{132}_{\rm ESS}}{v_2\left(\Delta\delta+\Delta\gamma^{132}_{\rm ESS}\right)}. \tag{9}$$

Figure 6 illustrates the beam-energy dependence of $\kappa^{112}_{\rm bg}$ and $\kappa^{132}_{\rm bg}$ for 20%–50% Au+Au collisions. Both $\kappa^{112}_{\rm bg}$ and $\kappa^{132}_{\rm bg}$ exhibit only weak dependence on beam energy and are consistent with values of approximately 2.5 and 1, respectively. This suggests that a universal coupling between elliptic flow and two-particle correlations can well describe the flow-related background. Accordingly, $\Delta\gamma^{112}$ and $\Delta\gamma^{132}$ share a common background mechanism, differing only in their coupling strengths. Therefore, once $\Delta\gamma^{132}_{\rm ESS}$ is reduced to zero, it is reasonable to infer that the flow-related background contribution to $\Delta\gamma^{112}$ is likewise effectively suppressed by the ESS method.

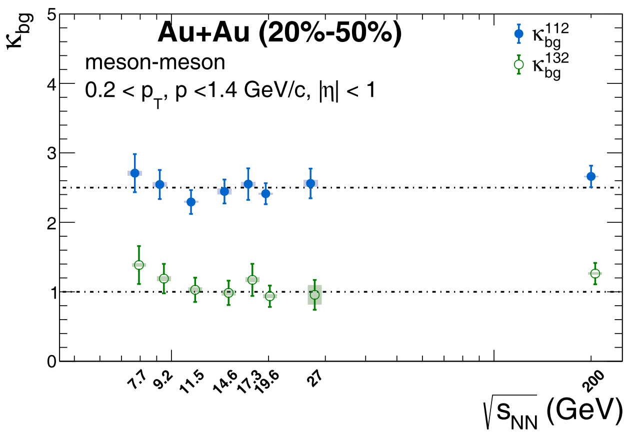

Fig. 6. (color online) Beam-energy dependence of $\kappa^{112}_{\rm bg}$ (full circles) and $\kappa^{132}_{\rm bg}$ (open circles) integrated over the 20%–50% centrality range in Au+Au collisions. Error bars represent statistical uncertainties, and shaded boxes denote systematic uncertainties. The dashed lines at 2.5 and 1 are drawn to guide the eye.

IV. CONCLUSION AND DISCUSSION

In summary, we have presented measurements of charge separation correlations along the magnetic field direction using Au+Au collisions at RHIC from $\sqrt{s_{NN}}$= 7.7 to 200 GeV energies, with the flow-related background effectively suppressed. We report a remaining charge separation signal in mid-central Au+Au collisions, positive finite with around 3σ significance at each of the center-of-mass energies of $\sqrt{s_{NN}}$= 11.5, 14.6, and 19.6

GeV. The results at $\sqrt{s_{NN}}$= 17.3 and 27 GeV also show positive values but with a lower significance of 1.3σ and 1.1σ. Below $\sqrt{s_{NN}}$= 10 GeV or at $\sqrt{s_{NN}}$= 200 GeV, the charge separation is consistent with zero. When the data between $\sqrt{s_{NN}}$= 10 and 20 GeV are combined, the significance rises to 5.4σ. Should future theoretical and experimental studies confirm that residual backgrounds are negligible, these measurements would constitute direct evidence for local $\mathcal{P}$ and $C\mathcal{P}$ violation in hot QCD matter: the first experimental probe of topological vacuum structure in a non-Abelian gauge theory.

The persistence of the charge separation signal $\Delta\gamma^{112}_{\rm ESS}$ in mid-central Au+Au collisions at beam energies between $\sqrt{s_{NN}}$= 10 and 20 GeV, and its absence at both lower and higher beam energies, warrant additional theoretical studies for these energies. Several theoretical mechanisms may contribute to this energy dependence. First, QCD topological vacuum transitions could be amplified near the conjectured critical point [59]. Second, the magnetic field lifetime may be longer at lower $\sqrt{s_{NN}}$ [60], matching the evolution time scale of the QGP phase, while at much higher energies the magnetic field, although stronger initially, would decay too rapidly compared to the QGP formation time to generate an observable CME [61, 62]. Finally, below $\sqrt{s_{NN}}$= 10 GeV, chiral symmetry restoration may be incomplete [63], weakening a key requirement for the CME, and the BES-II program does not have enough statistics at the low energy region to be conclusive.

The absence of a definitive CME signal at top RHIC and LHC energies [38, 64] provides constraints on the dynamical evolution of the magnetic field during the QGP phase. While both the magnetic field strength and chirality imbalance are expected to exhibit strong beam-energy dependence, the extracted flow-background coupling constants appear approximately universal, with $\kappa^{112}_{\rm bg} \approx 2.5$ and $\kappa^{132}_{\rm bg} \approx 1$. The electric charge separations obtained using the ESS method and the H correlator show excellent consistency.

These results place quantitative constraints on the magnetic field evolution in a QGP and the anomaly-driven charge transport at lower RHIC energies, providing the missing input for theoretical descriptions. They may also stimulate more searches for novel QCD phenomena, such as the chiral magnetic wave [65] inside QGP. Beyond heavy-ion collisions, it may inform the role of anomaly currents in systems ranging from the early Universe to strongly magnetized astrophysical matter, such as neutron stars [66, 67], which highlight the universal properties of chiral matter and topology in quantum many-body systems.

ACKNOWLEDGMENTS

We thank the RHIC Operations Group and SDCC at BNL, the NERSC Center at LBNL, and the Open Science Grid consortium for providing resources and support.

References

[1] D. Kharzeev, R. D. Pisarski, and M. H. G. Tytgat, Phys. Rev. Lett. **81**, 512 (1998)

[2] D. Kharzeev and R. D. Pisarski, Phys. Rev. D **61**, 111901(R) (2000)

[3] D. Kharzeev, Phys. Lett. B **633**, 260 (2006)

[4] Q. Li, D. Kharzeev, C. Zhang, *et al.*, Nature Phys **12**, 550 (2016)

[5] J. Xiong, S. K. Kushwaha, T. Liang, *et al.*, Science **350**, 413 (2015)

[6] X. Huang, L. Zhao, Y. Long, *et al.*, Phys. Rev. X **5**, 031023 (2015)

[7] D. E. Kharzeev and J. Liao, Nature Rev. Phys. **3**, 55 (2021)

[8] D. E. Kharzeev, J. Liao and P. Tribedy, Int. J. Mod. Phys. E **33**, 2430007 (2024)

[9] I. Arsene *et al.* [BRAHMS Collaboration], Nucl. Phys. A **757**, 1 (2005)

[10] B. B. Back *et al.* [PHOBOS Collaboration], Nucl. Phys. A **757**, 28 (2005)

[11] J. Adams *et al.* [STAR Collaboration], Nucl. Phys. A **757**, 102 (2005)

[12] K. Adcox *et al.* [PHENIX Collaboration], Nucl. Phys. A **757**, 184 (2005)

[13] S. Acharya *et al.* [ALICE Collaboration], Eur. Phys. J. C **84**, 813 (2024)

[14] A. Hayrapetyan *et al.* [CMS Collaboration], Phys. Rept. **1115**, 219 (2025)

[15] B. I. Abelev *et al.* [STAR Collaboration], Phys. Rev. Lett. **103**, 251601 (2009)

[16] B. I. Abelev *et al.* [STAR Collaboration], Phys. Rev. C **81**, 054908 (2010)

[17] L. Adamczyk *et al.* [STAR Collaboration], Phys. Rev. C **88**, 064911 (2013)

[18] B. Abelev *et al.* [ALICE Collaboration], Phys. Rev. Lett. **110**, 012301 (2013)

[19] M. S. Abdallah *et al.* [STAR Collaboration], Phys. Rev. C **105**, 014901 (2022)

[20] M. I. Abdulhamid *et al.* [STAR Collaboration] Phys. Rev. Res. **6**, L032005 (2024); Phys. Rev. C **110**, 014905 (2024).

[21] S. A. Voloshin, Phys. Rev. C **70**, 057901 (2004)

[22] S. Schlichting and S. Pratt, Phys. Rev. C **83**, 014913 (2011)

[23] S. Pratt, S. Schlichting and S. Gavin, Phys. Rev. C **84**, 024909 (2011)

[24] B. E. Aboona *et al.* [STAR Collaboration], Phys. Rev. C **113**, 014912 (2026)

[25] D. E. Kharzeev, L. D. McLerran, and H. J. Warringa, Nucl. Phys. A **803**, 227 (2008)

[26] V. Skokov, A. Illarionov, and V. Toneev, Int. J. Mod. Phys. A **24**, 5925 (2009)

[27] U. Heinz and R. Snellings, Ann. Rev. Nucl. Part. Sci. **63**, 123 (2013)

[28] S. Choudhury *et al.*, Chin. Phys. C **46**, 014101 (2022)

[29] J. Adam *et al.* [STAR Collaboration], Phys. Lett. B **798**,

134975 (2019)
[30] W.-T. Deng, X.-G. Huang, G.-L. Ma, and G. Wang, Phys. Rev. C **94**, 041901 (2016)
[31] R. Milton, G. Wang, M. Sergeeva, S. Shi, J. Liao, and H. Z. Huang, Phys. Rev. C **104**, 064906 (2021)
[32] L. Adamczyk *et al*. [STAR Collaboration], Phys. Rev. Lett. **113**, 052302 (2014)
[33] M. I. Abdulhamid *et al*. [STAR Collaboration], Phys. Rev. X **14**, 011028 (2024)
[34] H. Petersen, B. Müller, Phys. Rev. C, **88**, 044918 (2013)
[35] J. Schukraft, A. Timmins, S. A. Voloshin, Phys. Lett. B **719**, 394 (2013)
[36] S. Acharya *et al*. [ALICE Collaboration], Phys. Lett. B **777**, 151 (2018)
[37] S. Acharya *et al*. [ALICE Collaboration], J. High Energy Phys. **09**, 160 (2020)
[38] A. M. Sirunyan *et al*. [CMS Collaboration], Phys. Rev. C **97**, 044912 (2018)
[39] V. Khachatryan *et al*. [CMS Collaboration], Phys. Rev. C **92**, 034911 (2015)
[40] Z. Xu, B. Chan, G. Wang, A. Tang, H. Z. Huang, Phys. Lett. B **848**, 138367 (2024)
[41] M. Anderson *et al*., Nucl. Instrum. Meth. A **499**, 659 (2003)
[42] W. J. Llope *et al*. [STAR Collaboration], Nucl. Instrum. Meth. A **522**, 252 (2004)
[43] L. Adamczyk *et al*. [STAR Collaboration], Phys. Rev. C **86**, 054908 (2012)
[44] W.J. Llope *et al*. [STAR Collaboration], Nucl. Instrum. Meth. A **661**, S110 (2012)
[45] J. Chen *et al*., NUCL SCI TECH **35**, 214 (2024)
[46] L. Adamczyk *et al*. [STAR Collaboration], Phys. Rev. Lett. **110**, 142301 (2013)
[47] H. Bichsel, Nucl. Instrum. Meth. A **562**, 154 (2006)
[48] M. S. Abdallah *et al*. [STAR Collaboration], Phys. Rev. Lett. **128**, 092301 (2022)
[49] B. E. Aboona *et al*. [STAR Collaboration], Phys. Lett. B **839**, 137779 (2023)
[50] J. Adams *et al*. [STAR Collaboration], Nucl. Instrum. Meth. A **968**, 163970 (2020)
[51] C. Adler *et al*., Nucl. Instrum. Meth. A **470**, 488 (2002)
[52] S. Choudhury, G. Wang, W. B. He, Y. Hu and H. Z. Huang, Eur. Phys. J. C **80**, 383 (2020)
[53] Z. Xu, G. Wang, A. H. Tang, H. Z. Huang, Phys. Rev. C **107**, L061902 (2023)
[54] S. Shi, Y. Jiang, E. Lilleskov, J. Liao, Ann. Phys. **394**, 50 (2018)
[55] Z.-W. Lin, C.M. Ko, B.-A. Li, B. Zhang, S. Pal, Phys. Rev. C **72**, 064901 (2005)
[56] M. Stefaniak and H. Zbroszczyk1, EPJ Web of Conferences 164, **07013** (2017)
[57] R. Barlow, Conference on Advanced Statistical Techniques in Particle Physics, 2002, pp. 134–144.
[58] M. S. Abdallah *et al*. [STAR Collaboration], Phys. Rev. C **106**, 034908 (2022)
[59] K. Ikeda, D. E. Kharzeev, and Y. Kikuchi, Phys. Rev. D **103**, L071502 (2021)
[60] H. Li, X. Xia, X. G. Huang and H. Z. Huang, Phys. Rev. C **108**, 044902 (2023)
[61] L. Yan and X.-G. Huang, Phys. Rev. D **107**, 094028 (2023)
[62] D. Shen, J. Chen, X.-G. Huang, Y.-G. Ma, A. Tang and G. Wang, Research **8**, 0726 (2025)
[63] A. J. Mizher, M. N. Chernodub, and E. S. Fraga, Phys. Rev. D **82**, 105016 (2010)
[64] A. Shreyasi *et al*. [ALICE Collaboration], Phys. Lett. B **856**, 138862 (2024)
[65] Y. Burnier, D. E. Kharzeev, and J. Liao, Phys. Rev. Lett. **107**, 052303 (2011)
[66] J. Charbonneau and A. Zhitnitsky, JCAP **1008**, 010 (2010)
[67] Naoki Yamamoto, Phys. Rev. D **93**, 065017 (2016)